# Multi-barrel electrodes containing an internal micro-reference for the improved visualization of galvanic corrosion processes in magnesium-based materials using potentiometric scanning electrochemical microscopy

Dániel Filotás[1,2], Bibiana María Fernández-Pérez[3], Lívia Nagy[1,2], Géza Nagy[1,2], Ricardo M. Souto[3, 4]

[1] *Department for General and Physical Chemistry, Faculty of Sciences, University of Pécs, Ifjúság útja 6, 7624 Pécs, Hungary.*

[2] *János Szentágothai Research Center, University of Pécs, Ifjúság u.20. Pécs, 7624 Hungary.*

[3] *Department of Chemistry, Universidad de La Laguna, P.O. Box 456, E-38200 La Laguna, Tenerife, Canary Islands, Spain.*

[4] *Institute of Material Science and Nanotechnology, Universidad de La Laguna, E-38200 La Laguna (Tenerife), Spain.*

*****Corresponding authors:

Ricardo M. Souto, Department of Chemistry, Universidad de La Laguna, P.O. Box 456, E-38200 La Laguna, Tenerife, Canary Islands, Spain.
E-mail: rsouto@ull.es; Tel: +34 922 318067.

Géza Nagy, Department for General and Physical Chemistry, Faculty of Sciences, University of Pécs, Ifjúság útja 6, 7624 Pécs, Hungary.
E-mail: g-nagy@gamma.ttk.pte.hu.

## Abstract

Simultaneous monitoring of pH and $Mg^{2+}$ distributions above AZ63 magnesium alloy, either spontaneously corroding or galvanically coupled with iron, was achieved using SECM in the potentiometric operation. By introducing an internal micro-reference electrode in a multi-barrel arrangement of the ion-selective microelectrode used as scanning probe, superior performance was achieved compared to conventional single-barrel and double-barrel assemblies. In this way, the impact of the overestimated acidification accompanying metal dissolution using conventional tips was established from model experiments using non ion-sensitive open micropipettes and pH antimony microelectrodes. It is shown that the simultaneously acquired pH and pMg maps provide complementary information on the spontaneous and galvanic corrosion of AZ63 magnesium alloy.

**Keywords**: SECM; ion selective microelectrode; galvanic corrosion; pH distribution; Mg dissolution; magnesium.

## 1. Introduction

Magnesium is the fifth most abundant metal in the earth's crust and has a great biological importance and a wide variety of industrial applications. An example of applications is magnesium and its alloys are often used as sacrificial anodes due to their high reactivity. That is, when magnesium is in electrical connection with a less active metal in the electrochemical series and the two metals are immersed in the same electrolyte, its greater tendency to oxidation protects the nobler-metal cathode from dissolution. On the other hand, the main concern to use magnesium as a structural material is galvanic corrosion as well [1,2]. For these reasons, the galvanic corrosion of magnesium remains a hot topic among corrosion scientists. Recently, Esmaily et al. published a comprehensive review on the corrosion of magnesium [3], while Dauphine-Ducharme et al. reviewed surface scanning techniques as one of the most effective instrumental analysis families employed in corrosion research [4].

Similarly to what happened with the Scanning Vibrating Electrode Technique (SVET) [5-7] since 1989, the scanning electrochemical microscope (SECM) has become an attractive tool for corrosion scientists in recent years, as the SECM provides spatially-resolved chemical information of the reactions occurring at the solid-liquid boundary phase, opening new ways to characterize corroding surfaces [8-11]. When it comes to the investigation of magnesium corrosion, the amperometric mode of SECM is an efficient method of exploration [12], although Mg ions cannot be measured directly due to the high negative overvoltage of the $Mg^{2+}$ reduction [13]. Therefore, either the feedback mode [14] or hydrogen detection in sample generator – tip collector mode are the prevailing operation modes found in the literature [15-17]. However, it must be taken in account that the oxidation of $H_2$ is not a diffusion-controlled process in the strict sense, and that the local ion concentrations can affect the oxidation current [18]. Moreover, the hydrogen bubbles often cover parts of the magnesium surface wedging out-of-range values in the amperometric signal of the Pt microelectrode. Bubble formation also stirs the solution affecting the stability and resolution of the recorded image [19], and this feature remains an open challenge for all surface scanning techniques that operate in situ over magnesium and its alloys.

Alternately, SECM can also be employed in the potentiometric operation [20-23]. In this case, the sensing probe is an ion selective microelectrode (ISME), whose potential is measured against a reference electrode employing a voltage follower based on operational amplifiers. Several ionophores have been developed for $Mg^{2+}$ measurements, thus the advantage of

potentiometric SECM is the possibility of directly measuring $Mg^{2+}$ distributions [24,25]. Similar to the amperometric mode, the potentiometric SECM also faces some challenges, although some of them have been successfully overcome. Therefore, the use of solid contacts reduces the response time of the ISME, which allows obtaining less distorted concentration distribution images [26]. Next, at high scan rates, which are sometimes required to keep pace with the ongoing corrosion reactions, the images obtained can be deconvoluted to eliminate the distortion resulting from insufficient sampling time at each location [27]. However, some uncertainties have been observed in the quantitative evaluation of magnesium dissolution above galvanically corroding magnesium [28], namely unexpectedly low local pH values above defects over Mg coupled to galvanized steel which were attributed to metal hydrolysis [29]. More recently, an alternative explanation for those unrealistically big concentration changes was given in terms of the high electric field developed in the electrolytic phase during galvanic coupling [30]. Due to this electric field, the potential values measured at the ISME will be shifted with respect to those determined during the calibration step that is always carried out in unbiased condition. This reported shift accounts for the monitoring of unrealistically high metal ion activities in the adjacent solution to the corroding surface. For instance, $pMg<0$ values were obtained by extrapolation from the calibration plot, although they are physical impossibilities. In addition to describing the biasing effects of the electric field in the ISME recordings, in our previous work we also proposed a possible solution to overcome this limitation [30]. It consists of bringing the reference electrode as close as possible to the ISME by effectively reducing the potential difference that arises from the different locations of the electrodes in the electric field. In addition to achieving a minimum distance between these two electrodes, constrains to tip movement due to the presence of a fixed reference electrode in the electrolyte are avoided by using a multi-barrel arrangement for the manufacture of the tip. In fact, multi-barrel electrode arrangements are often employed to perform physiological measurements [31-35], as to eliminate the effects of neural activity [36]. More recently, we introduced multi-barrel electrode probes in SECM measurements to either achieve combined amperometric/potentiometric operation [37], or to monitor the concentration distributions of various chemical species over an actively corroding system [38]. Therefore, simultaneous pH and $Mg^{2+}$-ion concentration maps were recorded over a magnesium-iron galvanic pair [38]. In this stage, the possibility of using a multi-barrel arrangement to place the micro-reference electrode to only a few micrometers from

101 the measuring ion-selective microelectrode seems to be very advantageous for the investigation
102 of galvanic corrosion processes on magnesium-based materials due to the high electrical fields
103 developed by them [39].

104 As mentioned above, an additional advantage of multi-barrel electrode assemblies is the
105 possibility of simultaneous monitoring of different species which can provide deeper insight into
106 localized phenomena. Indeed, simultaneous measurements in corrosion science have been
107 attempted before, firstly by Karavai et al. [40], and then by others [41-43], although involving
108 separate single-electrode probes that were positioned close together employing dual stands [43].
109 In such arrangements, there was a finite separation between the probes that would not strictly
110 scan the same areas of the investigated surface unless sufficiently large scan lengths were
111 imposed to later correct for surface shifts. However, the unwanted contribution of the electric
112 field could not be eliminated in those arrangements, and the local acidification around anodic
113 spots remains to be overestimated in some cases. Although, for some purposes it is an elegant
114 and convenient way, the usage of multi-barrel electrodes would come with more benefits. Firstly,
115 incorporating multiple pipettes can be done nearly without limits, whereas the size of the
116 individual stages imposes a practical limitation to their number. For instance, it has been
117 described an assembly consisting of 9-barreled micropipettes that were employed for the
118 injection of different chemicals [44]. Yet, such a multi-channel monitoring in SECM
119 experiments would demand dedicate instrumentation. The second, and probably the most
120 important advantage of the multi-barrel arrangement, is the opportunity of a more precise
121 establishment of the tip-sample distance compared to the operation of separate single probes. The
122 common way to position a potentiometric probe at the desired distance from the surface
123 investigation is by using the "gentle approach" procedure. That is, a step-by-step approach of the
124 tip to the sample surface with an aid of a microscope is performed, and as the ISME abuts the
125 surface, the ISME can be lifted up from the surface to the desired tip-sample distance. In many
126 cases, however, this leads to the crash of the tip, as they are more fragile than the amperometric
127 probes. But instead of using liquid membrane pH sensitive microelectrodes, one can employ the
128 dual functioning antimony microelectrodes [45], which apart from potentiometric pH
129 measurements can be used for amperometric sensing of dissolved $O_2$ [46]. That is, prior to the
130 actual potentiometric measurements, amperometric *Z*-approach curves can be recorded to obtain
131 the corresponding feedback response, thus allowing establishing a precise tip-sample distance

without breaking the probe [47]. Subsequently, the potential of the antimony surface can be modified to be coated with a $Sb_2O_3$ film that is sensitive to pH [47]. Potentiometric mapping can be then performed using the same microelectrode [48]. However, the feedback mode requires the electrode surface to be parallel to the sample surface, which was not the case when using various single probes. Therefore, more precise tip-sample distance control by using multi-barrel assemblies is an additional feature for improved potentiometric SECM imaging.

In this paper we present a modified multi-barrel electrode assembly with respect to the double barrel arrangement reported in ref. [38]. The new design minimizes electric field distortion during the simultaneous imaging of $Mg^{2+}$ ions and pH distributions using potentiometric SECM from magnesium based materials under galvanic coupling conditions. Such improvement was attained by introducing a micro-reference electrode in the multi-barrel arrangement. Its advantageous characteristics for the simultaneous detection of dissolving $Mg^{2+}$ ions and the pH changes accompanying both the cathodic and anodic reactions, as well as the minimization of the electric fields contribution to the measured signals are demonstrated.

## 2. Experimental

### *2.1. Materials and solutions*

Sodium chloride and magnesium-chloride hexahydrate were supplied by Merck (Darmstadt, Germany). Antimony powder used for the preparation of pH sensitive antimony microelectrodes was purchased from Aldrich (Saint Louis, MO, USA). SECM measurements were conducted in 1 mM NaCl solution as test electrolyte. A set of magnesium-chloride solutions was employed for the calibration of the Mg ISME. They were prepared in tenfold dilutions of 0.1 M $MgCl_2$ solution, and the calibration sequence was initiated with the most diluted one, in $10^{-6}$ M concentration. Analogously, the antimony electrodes were calibrated in pH buffers ranging $4 \leq pH \leq 11$. Every solution was prepared using ultrapure water (resistivity, 18 MΩ cm; Millipore, Billerica, MA, USA). Micropipettes were fabricated by pulling borosilicate capillaries (outer diameter, Ø = 1.5 mm; internal diameter, Ø = 1.0 mm; Hilgenberg GmbH, Malsfeld, Germany), using a Narishige PE-2 pipette puller (Tokyo, Japan). Silanization of the capillaries was accomplished by soaking in 5% vol. solution of dichloro-dimethyl-silane in heptane (Sigma Aldrich) and then kept in oven at 120°C for 30 min. The carbon fibers for the solid contact were obtained as a generous gift from Specialty Materials (Lowell, MA, USA).

Magnesium alloy coupled to iron was used as model corrosion system. It was prepared from AZ63 alloy sacrificial boiler anode and 99.99% purity iron plates (Goodfellow, Cambridge, UK). Square base rods of 1 $mm^2$ cross section were cut from the boiler anode and the iron plate respectively, and one metal rod of each material was placed vertically within a home-made assembly to embed them in epoxy resin (EpofixKit, Struers, Denmark). The spacing between the AZ63 and Fe rods was ca. 5 mm spacing. Copper wires were welded to portions of the specimens protruding from the resin sleeve to provide electrical connection from the rear side of the mould, while the other end of the metal rods surrounded by the resin were exposed to the test electrolyte. The samples were ground using abrasive papers down to 4000 grit, and subsequently polished using Micropolish II Alumina Suspensions of 1 and 0.3 μm particle sizes (Buehler, Lake Bluff, IL, USA). The finished surfaces were thoroughly rinsed with Millipore deionized water, dried with ethanol, and finally surrounded laterally by Sellotape to create a small container for the test solution.

*2.2. Probe preparation*

Single-barrel electrodes were prepared as it is described in ref. [26]. The cocktail composition was: 1.5% bis-N,N, dicyclohexyl-malonamide ionophore, 2.6% high molecular weight polyvinyl chloride (PVC), 1.4% potassium tetrakis(4-chlorophenyl)borate, and 94.5 % ortho-nitrophenyl octyl ether. The solid contact of the ISME were made using carbon fibers (30 μm dia.) coated by poly-3,4-ethylenedioxythiophene (PEDOT). After the tips were backfilled with the ion selective cocktail, the PEDOT coated carbon fibre was dipped inside the cocktail to such an extent as to be proximate to the orifice of the micropipette.

The preparation of the antimony fibre microelectrodes responsive to pH, with diameter in the micrometer scale, was described in detail elsewhere [20]. In brief, molten antimony was sucked into a capillary, and the glass-surrounded antimony wire was then subjected to successive pulling procedures until fibres of the desired diameter (5-15 μm) were prepared. The antimony fibre was then glued at its rear side in the lumen of the capillary, and the electric connection was begotten using mercury and a copper wire.

The preparation of double- and triple-barrel electrode probes were initiated by attaching together the chosen number of single-barrel borosilicate capillaries. The capillaries were subsequently placed in the vertical puller provided with a rotary chuck, the puller was splayed,

and the coil was heated for the capillaries to be twirled while the chuck was rotated. This step allowed the individual capillaries to be merged into one single body. In a second heating stage, the splay was removed, and two sharp multi-barrel capillaries were produced while pulling. The capillaries were selectively silanized using a homemade chamber containing the silanization agent. A tube penetrates the cap of the chamber and fits perfectly into the barrel intended to contain the ISME, allowing thus the chamber to be connected solely to the selected barrel. The reference and the antimony containing barrels were filled with water to prevent them from the silanizing agent penetrating through the orifice of the tip. Then, the system was placed into the furnace for 1 h at 50°C. The micro-reference barrel was filled with 0.1 M KCl solution and a chlorinated silver wire was dipped into it. The antimony fibre was introduced inside the other barrel, and inserted towards the end of the tip using metallic wires. When the fibre protruded through the orifice, it was pulled until it got stuck in it. Then, the protruding portion of the antimony fibre was eventually cut. The electric connection was facilitated using liquid mercury and a copper wire. The Mg ISME barrel was backfilled with about 10 μL of the ion selective cocktail, and then a PEDOT-coated carbon fibre of 30 μm diameter was positioned as close as possible to the orifice. Usually the liquid column between the orifice and the end of the carbon fibre was about 1-2 mm high. A schematic drawing and two micrographs of the triple-barrel electrode are shown in Figure 1. The calibration curves of the Mg-ISME and the pH sensitive antimony microelectrodes are shown in the Supplementary material.

In addition, a single-barrel scanning micro-reference electrode was also employed to sense the local potential distributions produced in the electrolyte volume adjacent to an actively corroding sample. A chlorinated silver wire was introduced in the lumen of an open micropipette filled with 0.1 M KCl solution, and its potential was monitored with respect to a conventional Ag/AgCl/(3M) KCl reference placed at a fixed position in the bulk of the electrolyte, approximately 1-1.5 cm away from the travelling microelectrode probe. The diameter of the orifice was smaller than 15 μm, small enough to neglect possible effects due to the diffusion of potassium ions within the timeframe of the measurements. The vertical tip-sample distance was established using the “gentle approach”, followed by controlled removal from the surface to a height of 20 μm, and then the sample was scanned parallel to its surface at 20 μm $s^{-1}$ scan rate and 50 μm step size.

### *2.3. Scanning Electrochemical Microscopy*

SECM experiments were performed using an instrument manufactured by Sensolytics (Bochum, Germany) and operated with an Autolab bipotentiostat (Metrohm Autolab BV, Utrecht, The Netherlands), all controlled with a personal computer. A homemade voltage follower based on a $10^{12}$ Ω input impedance operational amplifier (mod. TL071, Texas Instruments, Dallas, TX, USA) was interconnected between the cell and the potentiometric input of the system. The electrochemical cell was completed with an Ag/AgCl/(3 M) KCl electrode as reference ($E^0$ = +0.197 V vs. NHE), or with the micro-reference electrode introduced in the multi-barrel assembly. If not stated otherwise, the scans were performed at 20 μm height from the sample with 17 μm $s^{-1}$ nominal scan rate, and 50 μm step size. The tip-sample vertical distance was established by recording amperometric *Z*-approach curves using the antimony barrel biased at -0.70 V vs. Ag/AgCl/(3 M) KCl, whereas the "gentle approach" was employed for the single barrel electrodes. Photographs of the samples after SECM testing were taken *ex situ* after the test electrolyte was spilled from the cell, gently washing of the sample with deionized water, and sample drying in air.

## 3. Results and discussion

The performance of the multi-barrel probe assembly for the characterization of the galvanic corrosion of magnesium and its alloys was tested on a model AZ63 alloy-iron pair. The SECM data on the dissolution of $Mg^{2+}$ and the pH changes accompanying the anodic and cathodic half cell reactions were monitored using either multi-barrel electrode arrangements or conventional single barrel probes for comparison. Figure 2 shows typical pH and pMg maps recorded above a spontaneously corroding magnesium alloy strip immersed in 1 mM NaCl solution that were measured using single barrel microelectrodes. Tip replacement was required between both scans. According to Figure 2A, the electrolyte directly in contact with the surface of AZ63 became alkaline over the metal, as would be expected from the cathodic half-cell reaction. Although the anodic process can occur in a localized way on the spontaneously corroding metal in chloride-containing solution, the featureless pH distribution did not allow the detection of the corresponding anodic sites. In other words, the pH changes caused by the hydrogen evolution reaction greatly exceeded those associated to the hydrolysis of the dissolved metal ions. In this pH map, only the surrounding resin could be distinguished from the metal

surface due to the appearance of lower pH values, although pH values close to neutrality were only reached at a greater distance from the metal. In contrast, the $Mg^{2+}$ map given in Figure 2B shows a highly localized distribution of these ions over the surface of the alloy. The anodic activity related to two active anodic sites could be distinguished on the right side of the sample. Almost one unit change pMg occurred at the most active site indicated by the arrow drawn in Figure 2B. These features were supported by taking an optical micrograph after the sample was removed from the electrolyte as shown in Figure 2C. That is, at the location where the magnesium dissolution preferentially occurred according to the pMg map of Figure 2B, the optical micrograph showed a hole in the metal sample, which was coated by a dark bilayer of $MgO/Mg(OH)_2$ and surrounded by particles of other corrosion products. In contrast, the remaining surface did not show a significant degradation of the material, correlating well with the values of pMg in the SECM map near the lower detection limit of the Mg-ISME.

As mentioned in Section 1, spurious contributions to potential can arise from the electric field developed in the electrolyte phase while Mg and Fe are electrically connected and immersed in the same electrolyte. As a result, the potential measured by the ISME would not only comprise the Nernstian's response to the ions of interest, but also the difference in electrical potential experienced by the reference and the measuring electrodes. The possible occurrence of a potential bias on the surface of the magnesium alloy due to the formation of local galvanic pairs on the metal under spontaneous corrosion conditions was investigated next. In this case, an Ag/AgCl micro-reference electrode filled with 0.1 M KCl solution was used as the scanning probe. It should be noted that such a probe of this type would be insensitive to changes in ion activities, although changes similar to those caused by an electric field effect would be detected by measuring its potential against a conventional Ag/AgCl/(3M) KCl reference electrode. The diameter of the orifice was smaller than 15 μm, small enough to neglect the eventual effects due to the diffusion of potassium ions within the duration of the measurements. Potential distribution maps were recorded above the AZ63 strip under both open circuit and galvanic coupling conditions, and are shown in Figure 3. They were recorded using the following scan conditions: vertical sample-tip distance, 20 μm; step size, 50 μm; and scan rate, 20 μm $s^{-1}$. A slow shift of the potential values towards more negative potentials was observed while scanning the AZ63 sample that was spontaneously corroding in the test electrolyte (see Figure 3A), although it reached a steady constant potential after recording a few lines. The total potential variation

287 recorded above the AZ63 strip was only 1-1.5 mV. However, a change of approximately 75 mV
288 was recorded above the AZ63 strip after the galvanic coupling to the iron sample, a potential
289 change that would correspond to a change in magnitude in the ionic activity of approximately
290 2.4-2.7 orders according to the calibration plot of the Mg ISME. This experiment supports that
291 sufficiently reliable measurements can be performed using a single-barrel ISME under
292 conditions of spontaneous corrosion. On the contrary, in the case of galvanic coupling, the
293 increase in the dissolution rate of magnesium can be overestimated to a large extent using the
294 same probes. Therefore, the remaining experiments involving the AZ63-Fe galvanic couple were
295 performed using multi-barrel microelectrode probe arrangements containing a micro-reference
296 electrode in the vicinity (<10 μm) of the measuring ion-selective micropipette or the antimony
297 electrode.

298 Next, the pH distributions recorded above the AZ63 strip electrically connected to the
299 iron for a galvanic pair in 1 mM NaCl solution were recorded using the antimony microelectrode
300 included in a double-barrel probe containing an internal micro-reference in the other barrel. For
301 the sake of comparison, the potential of the antimony microelectrode was measured first with
302 respect to the micro-reference electrode contained in the double-barrel, while in the subsequent
303 scan the potential values were recorded with respect to a conventional Ag/AgCl/(3M) KCl
304 reference electrode placed in the bulk of the electrolyte. Although the time required to change the
305 electrical connector for the reference electrode only lasted a few seconds, and the two line scans
306 were performed over the same locations in the sample, pH ranges and pH distributions markedly
307 different were recorded above the AZ63 strip and the surrounding resin in each case as shown in
308 Figure 4. When the measurement was made against the internal micro-reference electrode, the
309 electrolyte volume adjacent to the AZ63 strip showed pH values close to neutrality, i.e., slightly
310 more alkaline than the naturally aerated initial test solution. There was approximately one pH
311 unit change over the AZ63 sample, with a small decrease in pH approximately over the centre of
312 the metal strip, which is assumed to be due to hydrolysis of magnesium above an actively
313 dissolving anodic site. Next, as the scanning probe translates from the metal to the surrounding
314 resin, the pH values quickly returned to the same background level previously observed at the
315 beginning of the line scan while travelling over the resin on the opposite side. However, when
316 the conventional reference electrode in the bulk of the test solution was employed instead, a very
317 different pH distribution was obtained. First, the solution away from the metal strips showed a

bulk acid pH value of 5.3. Then, the pH became even more acidic (namely, 4.7) when the probe passed over the magnesium alloy. Such acid pH should be considered an artefact because the hydrolysis of $Mg^{2+}$ cannot sustain such behaviour. That is, when the anodic dissolution of magnesium and its subsequent hydrolysis is written according to equations (1) and (2):

$$Mg \rightarrow Mg^{2+} + 2e^{-} \quad (1)$$

$$Mg^{2+} + n\,H_2O \rightarrow \left[Mg(OH)_n\right]^{(2-n)+} + n\,H^{+} \quad (2)$$

the corresponding hydrolysis constant for $n = 2$ is given by:

$$pK_{hyd} = 2\,pH + \log\left[Mg^{2+}\right] \quad (3)$$

By taking $pK_{hyd} = 11.4$ [49], and assuming $Mg^{2+}$ concentrations up to 1 M, it has been shown that the hydrolysis of $Mg^{2+}$ ions cannot originate pH values below 5.3 [50].

Furthermore, after reaching the unlikely value of pH 4.75, the pH monitored by the antimony microelectrode returned to values similar to those measured on the other side of the sample, although a new artefact appeared around $X = 2400$ μm. This demonstrates the superior performance of the multi-barrel microelectrode arrangement for SECM imaging of the galvanic corrosion of magnesium-based materials.

Figure 5 shows a 2D map of the pH distribution developed above all the surface of the AZ63 alloy exposed to 1 mM NaCl while galvanically connected to an iron rod. This image was obtained using a double-barrel probe containing the antimony and the micro-reference electrodes to minimize bias of the electric field that arises from the incorrect disposition of the electrodes in the small electrochemical cell. It should be noted that the magnesium dissolution is expected to be faster in the galvanic coupling condition and, therefore, a slight acidification arising from the hydrolysis of $Mg^{2+}$ ions can be expected. In fact, the pH map of Figure 5B shows that the volume of electrolyte adjacent to most of the AZ63 surface became alkaline, similar to the alkalization observed during the spontaneous corrosion of this material in the same electrolyte (cf. Figure 2A). However, in the lower region of the image a distinctive anodic behaviour was recorded which resulted in a weak acidification of the adjacent electrolyte. The occurrence of preferential metal dissolution and the subsequent deposition of corrosion products in this region was confirmed by inspection of the micrograph depicted in Figure 5B. This anodic feature could not

346 be seen in the case of spontaneous corrosion, because the alkalization due to the cathodic
347 reaction exceeded the weaker acidification resulting from the anodic sites. Here, it can be seen
348 that the enhanced magnesium dissolution produces an effective local acidification, which could
349 be resolved from the predominantly alkaline distribution developed above the sample. It should
350 be noted that the local acidification monitored in this map did not fall below pH = 6.4, which
351 agrees well with the previous comments on the hydrolysis of the $Mg^{2+}$ species and its effect on
352 the lowest possible pH value.
353 The same experiment was repeated using a different double-barrel probe containing an
354 Mg-ISME instead of the antimony ME in addition to a micro-reference electrode. Figure 6 shows
355 the registered pMg map and a micrograph of the AZ63 strip. The 2D scan was recorded shortly
356 after the immersion of the freshly finished sample in the test electrolyte. The approximate
357 position of the sample on the pMg map was indicated by drawing the contour of the sample. pMg
358 values near the lower detection limit of the ISME were measured above the resin surrounding the
359 magnesium alloy. A highly localized magnesium dissolution that produced the lowest pMg
360 values was recorded over the lower portion of the AZ63 strip, which led to a decrease of 4 units
361 for pMg compared to the values recorded above the resin. This behaviour was the consequence
362 of the enhanced dissolution of magnesium due to the galvanic coupling of AZ63 to iron. Such
363 enhanced dissolution rates in the lower part of the exposed AZ63 strip were confirmed by the
364 optical micrograph given in Figure 6B. The most degraded region in the sample covered an area
365 with a contour very similar to that in the pMg map exhibiting pMg values smaller than 3. In fact,
366 the triangular contour drawn in these images surrounds a region that exhibited numerous cavities
367 in the micrograph, although they were more noticeable in those regions that delivered the highest
368 concentration of $Mg^{2+}$ in the pMg map (i.e., near the bottom of the sample). Another region of
369 enhanced anodic activity leading to magnesium dissolution was also observed in the upper left of
370 the pMg map and the optical micrograph, confirming the good resolution of the potentiometric
371 SECM to resolve *in situ* the localized nature of the corrosion process. The only apparent
372 exception to this proposal was found in the upper right corner of the sample when comparing the
373 pMg map and the micrograph. That is, a relatively large hole could be observed in the optical
374 micrograph, while the pMg map showed no change in the concentration of $Mg^{2+}$ species in that
375 location. A possible justification for this feature can be made in terms of the relatively long time
376 it takes to scan the whole image using potentiometric SECM. The scan was initiated in the lower

left corner of the image from left to right. Therefore, when the scanning probe reached the aforementioned area, most likely developed shortly after immersion of the sample in the test electrolyte, that anodic site could already have been repassivated due to the precipitation of magnesium oxy-hydroxides. In fact, one has to make a compromise between fast scan rates and high resolution when it comes to potentiometric SECM. However, this map represents a significant improvement in spatial resolution compared to those previously reported using single-barrel probes, where there was only a large red spot (with respect to the colour scale used here) that gave pMg values outside the linearity range of the ISME [30].

The simultaneous measurement of $Mg^{2+}$ and pH distributions above AZ63 that spontaneously corrode in 1 mM NaCl was carried out using a triple-barrel arrangement containing the Mg ion selective and the antimony microelectrode probes, as well as an internal micro-reference electrode. The corresponding scan maps are shown in Figure 7 together with an optical micrograph of the sample. As was observed previously in the case of the sample that corrodes spontaneously, the alkalization derived from the evolution of hydrogen evolution in the local cathodes exceeded the local decrease in pH in the vicinity of the anodic sites. The total changes of pH and pMg also are in good agreement with the measurements made with single-barrel electrodes, that is, the pMg change did not exceed 1 unit, while the highest pH values approached 9 at 20 μm vertical tip-sample distance after 30-45 min exposure. The red arrows drawn in Figures 7A and 7C are pointing to those areas of high magnesium activity that corresponded to the formation of black deposits on the surface of the metal. Notable degradation of the AZ63 sample could be observed in the upper right part of the image; however, significantly enhanced values of $Mg^{2+}$ were not detected using the Mg ISME barrel at that location. The reason for this apparent discrepancy can be given in terms of the same reason used for the pMg map of Figure 6A; that is, the anodic areas activated at the beginning of the scan could have lost their anodic activity during the time required to register the complete SECM map. Therefore, if they occurred on the opposite side at the start of the scan, they might not show any detectable increase in concentration at the time the tip arrived there due to diffusion. However, some alkalization was still noticeable in that location on the pH distribution map given in Figure 7B (see the upper left blue arrow), which is in good agreement with the observation of greater cathodic activity ion the black spots that previously were anodic areas. The upper right arrow indicates a cathodic site, just next to the anodic site (top right red arrow on the upper right

in Figure 7A), which also agrees with literature reports using the scanning vibrating electrode technique (SVET) [51]. Finally, the arrow in the lowerleft indicated a high activity cathodic area, in which the surface of the metal exhibited a relatively smooth morphology in the optical micrograph, as well as the absence of anodic dissolution according to the corresponding pMg map.

The triple-barrel probe was also used to characterize the AZ63 alloy galvanically coupled to the iron during immersion in a 1 mM NaCl solution to simultaneously obtain the pH and pMg distributions over the magnesium alloy. In this case, successive line scans over arbitrarily selected lines crossing over the AZ63 strip were recorded, which allowed to follow the changes in the electrochemical activity of the surface to be followed over time, and four of them are displayed in Figure 8. To facilitate the comparison of the pH and pMg spatial distributions, the pMg scale has been inverted in the plots, so that the local maxima and minima represent a high and low $Mg^{2+}$ activity, respectively. The choice of recording line scans instead of the 2D maps that extend over the overall AZ63 alloy sample was taken this time because the increased rates of anodic dissolution spreading over a more extended surface should occur under a galvanic coupling condition compared to the spontaneous corrosion just described, while the travelling distance along the *X* axis could not be modified to combine a high resolution with a short measurement duration. It should be remembered that, in the case of the 2D map shown in Figure 6, the detection of an anodic area was missed due to long duration of the complete scan.

The line scans for the pH and pMg distributions displayed in Figure 8A indicate that metal dissolution occurred in a highly localized manner, showing an acute peak in the pMg plot at a location near the left edge of the sample. This high local concentration of $Mg^{2+}$ ions was accompanied by a minimum in the pH graph, with values very close to neutrality. The local pH decrease resulted from the hydrolysis of the released metal ions associated with the detection of an active anodic site. Further excursion of the probe to the right side led to an abrupt decrease in the concentration of dissolved metal, while the alkalization of the electrolyte occurred with almost the same path. The pH values monitored on the right side of the sample levelled off at ca. 8.6, and decreased slowly when the probe travelled to the surrounding resin. The lowest pMg values in this line scan were recorded in this region, despite the agitation of the solution caused by the movement of the probe from left to right. It can be deduced that the metallic surface adjacent to the anodic site behaves like a local cathode that allows a portion of the electrons

released by magnesium dissolution to be available for the anomalous hydrogen evolution effect, although most of the cathodic activity would preferentially occur in the iron strip. This observation is in good agreement with reports of enhanced evolution of hydrogen on anodically polarized magnesium [51-54], a feature that suggests that catalytic effects towards hydrogen evolution are exhibited by either the active film-free magnesium surface [55,56], or the oxy-hydroxide layer developed in the anodic reaction [57-59].

Similar trends can be observed for the pMg and pH distributions recorded over the AZ63 sample in the plots of Figure 8B. The anodic activity was observed on the left side of the metal strip as before, although in this case the pMg values corresponded to an order of magnitude decrease in the concentration of the metal ion. The line scan showed values close to pMg ≈ 4 over the resin at left of the metal strip, which is about 1 order of magnitude higher than the lower limit of detection. The occurrence of finite concentrations of the $Mg^{2+}$ ion over the resin can be justified by the increased rate of the magnesium dissolution and the subsequent diffusion of $Mg^{2+}$ ions to the surrounding resin areas. Correspondingly, a plateau displaying slightly acid pH values related to anodic activity in the metal sample was monitored both over the resin and over the metal strip on the left side. As the probe approached the centre of the alloy strip, there was both a decrease in the concentration of the metal ion and the alkalization of the adjacent electrolyte, the latter corresponding to an increase in pH to ca. 10 around 1250 μm on the *X* scale. It should be noted that the highest pH values were reached in the same region that had the highest pMg values that could be detected with the probe. The enhanced hydrogen evolution should account for these observations in a manner similar to the line scan in Figure 8A, although lower concentrations of the $Mg^{2+}$ ion and higher pH values were observed on the right side of the line scans in Figure 8B. Since this pH value could not account for the observed decrease of an order of magnitude of dissolved $Mg^{2+}$ activity, then a decreased activity of the anodic dissolution reaction at that location must be assumed, while there was an increase in activity of the hydrogen evolution reaction. This result would be an additional confirmation of the observation by Williams et al. that the anodic regions eventually become local cathodes over time [57]. The cathodic activation of the former anodes occurs even under anodic polarization, which is usually invoked to explain the anomalous hydrogen evolution on anodically polarized magnesium [57]. Further excursion of the probe to the right led to a decrease in the pH and pMg values,

effectively approaching the values that were recorded above the resin on the opposite side of the AZ63 strip.

The line scan depicted in Figure 8C introduced a new situation in which the pH and the $Mg^{2+}$ activity increased simultaneously over the magnesium alloy. This is an apparent contradiction with the line scans given in Figure 8 A and 8B, and represents the first report of such behaviour due to the lack of true simultaneous pH and pMg monitoring over galvanically corroding magnesium in the literature so far. However, the magnitude of the pH increase and its maximum values do not directly contradict the pMg values. Rather, it evidenced that anodic and cathodic sites can occasionally be very close to each other on the corroding surface, as seen in Figure 7. In addition, the local pMg minimum at the centre of the AZ63 strip suggests that there were two anodic sites in the edges of the sample, while in the centre there was a region that presents increased hydrogen evolution activity. The maximum of the pH and the minimum of pMg coincide well, confirming the previous assumption. However, the hydrogen source in the centre did not evolve sufficiently to significantly modify the pH distribution above the resin, although the vigorous dissolution of magnesium led to the measurement of somewhat higher pMg values above the surrounding resin as well.

Another particular pair of pMg and pH profiles is shown in Figure 8D. The largest activities of magnesium ions recorded so far were observed at the left edge of the magnesium alloy, with an abrupt decrease of 3 orders of magnitude around 600 μm. It is not surprising, since the pH reaches its highest alkalization with a maximum around pH = 11. In the case of such alkaline solution, the dissolved $Mg^{2+}$ level can not exceed ~$10^{-5}$ M. In fact, the pMg value rapidly dropped to almost the lower limit of detection of the Mg-ISME. Then a local minimum was observed in the pH line accompanied by a local maximum in $Mg^{2+}$ activity. It must be taken in account that the pH value contradicts the measured amount of $Mg^{2+}$. A possible justification may be based on the observation of a second pH maximum after this local minimum, which implies that he actual pH value may not have been reached at the minimum due to the short equilibration time. This was the case previously with the minimum of pMg recorded at $X \approx 600$ μm. Although the pH values suggest a pMg value around 5, the Mg-ISME barrel travelled farther, near to another local anode around $X \approx 850$ μm, which counteracted the decrease due to the alkaline environment. However, at the second pH maximum, the pMg value reached the limit of detection for the Mg ISME, since the second pMg maximum amounted to 3 and the change was

significantly lower than in the first case when pMg = 1. Finally, further excursion of the combined Mg-ISME and antimony probe to the right showed that the pMg and pH distributions relaxed towards the bulk levels recorded over the resin.

Finally, although a possible interference of $Mg^{2+}$ ions on the pH selectivity of the Sb microelectrode cannot be discarded at this stage, the multibarrel arrangement containing the Mg-ISME and the $Sb/Sb_2O_3$ microelectrodes allows eventual correction of the measured activity data. The correction procedure would involve the arrangement of an equation system containing the same number of unknowns and equations, as it was already done for an assembly of Zn- and Cu-ISME's in ref. [60].

## 4. Conclusions

In this contribution, a new multi-barrel assembly for potentiometric SECM imaging of galvanic corrosion processes at magnesium and its alloys that effectively eliminates electric field effects has been presented. This probe allows a real simultaneous detection of dissolved magnesium and pH changes to be performed with high chemical and spatial resolution. It consists of housing a solid-contact ion-selective $Mg^{2+}$ selective microelectrode, a pH sensitive antimony microelectrode, and an Ag/AgCl micro-reference electrode in a single multi-barrel body. The introduction of a micro-reference electrode into the body of the multi-barrel electrode effectively helped to overcome the undesired contribution of the electric field to the signal measured by establishing the galvanic coupling condition. The mapping of the electric potential changes above a sample of AZ63 magnesium alloy under conditions of spontaneous or galvanically coupled corrosion conditions showed that the spontaneous corrosion was slightly affected by the electric field developed around local anodes and cathodes, while leading to a severe distortion of measurements in galvanic corrosion condition. In addition to the improved chemical resolution, a true simultaneous measurement of several chemical species can be achieved. The simultaneous measurements confirm that the local pH greatly influences the dissolved $Mg^{2+}$ measurements; therefore, magnesium corrosion cannot be interpreted exclusively when performing pMg measurements, even if the effects of the electric field were effectively avoided.

## Acknowledgements

D. Filotás expresses his greatest gratitude to the ERASMUS+ program for the financial support of a 2-month mobility grant to the University of La Laguna. B.M. Fernández-Pérez is grateful to the Canarian Agency for Research, Innovation and Information Society (Las Palmas de Gran Canaria, Spain) and the European Social Fund (Brussels, Belgium) for a research contract. Financial support by the Spanish Ministry of Economy and Competitiveness (MINECO, Madrid) and the European Regional Development Fund, under grant CTQ2016-80522-P, The National Research, Development and Innovation Office (Budapest, Hungary) under grant K125244 is gratefully acknowledged.

## References

1. G. Song, A. Atrens, Understanding magnesium corrosion – framework for improved alloy performance, Adv. Eng. Mater. 5 (2003) 837-858.
2. G. Song, B. Johannesson, S. Hapugoda, D. StJohn, Galvanic corrosion of magnesium alloy AZ91D in contact with an aluminum alloy, steel and zinc, Corros. Sci. 46 (2004) 955-977.
3. M. Esmaily, J.E. Svensson, S. Fajardo, N. Birbilis, G.S. Frankel, S. Virtanen, R. Arrabal, S. Thomas, L.G. Johansson, Fundamentals and advances in magnesium alloy corrosion, Prog. Mater. Sci. 89 (2017) 92–193.
4. P. Dauphin-Ducharme, J. Mauzeroll, Surface analytical methods applied to magnesium corrosion, Anal. Chem. 87 (2015) 7499-7509.
5. H.S. Isaacs, The measurement of the galvanic corrosion of soldered copper using the scanning vibrating electrode technique, Corros. Sci. 28 (1988) 547-558.
6. R.M. Souto, J. Izquierdo, J.J. Santana, S. González, Scanning microelectrochemical techniques: a sensitive route to evaluate degradation reactions and protection methods with chemical selectivity, Eur. J. Sci. Theol. 9 (2013) 71-89.
7. K.B. Deshpande, Effect of aluminium spacer on galvanic corrosion between magnesium and mild steel using numerical model and SVET experiments, Corros. Sci. 62 (2012) 184–191.
8. C.H. Paik, H.S. White, R.C. Alkire, Scanning electrochemical microscopy detection of dissolved sulfur species from inclusions in stainless steel, J. Electrochem. Soc. 147 (2000) 4120–4124.

9. N. Casillas, S.J. Charlebois, W.H. Smyrl, H.S. White, Scanning electrochemical microscopy of precursor sites for pitting corrosion on titanium, J. Electrochem. Soc. 140 (1993) L142–L145.
10. A. Simões, D. Battocchi, D. Tallman, G. Bierwagen, Assessment of the corrosion protection of aluminium substrates by a Mg-rich primer: EIS, SVET and SECM study, Prog. Org. Coat. 63 (2008) 260–266.
11. A.M. Simões, A.C. Bastos, M.G. Ferreira, Y. González-García, S. González, R.M. Souto, Use of SVET and SECM to study the galvanic corrosion of an iron–zinc cell, Corros. Sci. 49 (2007) 726–739.
12. S.S. Jamali, S.E. Moulton, D.E. Tallman, M. Forsyth, J. Weber, G.G. Wallace, Applications of scanning electrochemical microscopy (SECM) for local characterization of AZ31 surface during corrosion in a buffered media, Corros. Sci. 86 (2014) 93-100.
13. S. Thomas, J. Izquierdo, N. Birbilis, R.M. Souto, Possibilities and limitations of scanning electrochemical microscopy of Mg and Mg alloys, Corrosion 71 (2015) 171-183.
14. X. Liu, T. Zhang, Y. Shao, G. Meng, F. Wang, Effect of alternating voltage treatment on the corrosion resistance of pure magnesium, Corros. Sci. 51 (2009) 1772–1779.
15. S.S. Jamali, S.E. Moulton, D.E. Tallman, M. Forsyth, J. Weber, G.G. Wallace, Evaluating the corrosion behaviour of magnesium alloy in simulated biological fluid by using SECM to detect hydrogen evolution, Electrochim. Acta 152 (2015) 294–301.
16. U.M. Tefashe, M. E. Snowden, P. Dauphin, M. Danaie, G.A. Botton, J. Mauzeroll, Local flux of hydrogen from magnesium alloy corrosion investigated by scanning electrochemical microscopy, J. Electroanal. Chem. 720–721 (2014) 121–127.
17. E. Mena-Morcillo, L.P. Veleva, D.O. Wipf, Multi-scale monitoring the first stages of electrochemical behavior of AZ31B magnesium alloy in simulated body fluid, J. Electrochem. Soc. 165 (2018) C749-C755.
18. D. Zhan, J. Velmurugan, M.V. Mirkin, Adsorption/desorption of hydrogen on Pt nanoelectrodes: Evidence of surface diffusion and spillover, J. Am. Chem. Soc. 131 (2009) 14756-14760.
19. J. Izquierdo, B.M. Fernández-Pérez, D. Filotás, Z. Őri, A. Kiss, R.T. Martín-Gómez, L. Nagy, G. Nagy, R.M. Souto, Imaging of concentration distributions and hydrogen evolution

on corroding magnesium exposed to aqueous environments using scanning electrochemical microscopy, Electroanalysis 28 (2016) 2354-2366.

20. J. Izquierdo, L. Nagy, I. Bitter, R.M. Souto, G. Nagy, Potentiometric scanning electrochemical microscopy for the local characterization of the electrochemical behaviour of magnesium-based materials, Electrochim. Acta 87 (2013) 283–293.
21. R. M. Souto, A. Kiss, J. Izquierdo, L. Nagy, I. Bitter, G. Nagy, Spatially-resolved imaging of concentration distributions on corroding magnesium-based materials exposed to aqueous environments by SECM, Electrochem. Commun. 26 (2013) 25–28.
22. P. Dauphin-Ducherme, R.M. Asmussen, D.W. Shoesmith, J. Mauzeroll, In-situ $Mg^{2+}$ release monitored during magnesium alloy corrosion, J. Electroanal. Chem. 736 (2015) 61-68.
23. S.H. Salleh, N. Birbilis, M. Musameh, K. Venkatesan, S. Thomas, On the development and application of an in-house fabricated $Mg^{2+}$ ion selective microelectrode (ISME) for assessing Mg corrosion, J. Electrochem. Soc. 165 (2018) C771-C776.
24. J. O'Donnell, H. Li, B. Rusterholz, U. Pedrazza, W. Simon, Development of magnesium-selective ionophores, Anal. Chim. Acta 281 (1993) 129-134.
25. N.A. Chaniotakis, J.K. Tsagatakis, E.A. Moschou, S.J. West, X. Wen. Magnesium ion-selective electrode: optimization and flow injection analysis application, Anal. Chim. Acta 356 (1997) 105-111.
26. J. Izquierdo, A. Kiss, J.J. Santana, L. Nagy, I. Bitter, H.S. Isaacs, G. Nagy, R.M. Souto, Development of $Mg^{2+}$ ion-selective microelectrodes for potentiometric scanning electrochemical microscopy monitoring of galvanic corrosion processes, J. Electrochem. Soc. 160 (2013) C451-C459.
27. A. Kiss, G. Nagy, Deconvolution of potentiometric SECM images recorded with high scan rate, Electrochim. Acta 163 (2015) 303-309.
28. R.M. Souto, A. Kiss, J. Izquierdo, L. Nagy, I. Bitter, G. Nagy, Spatially-resolved imaging of concentration distributions on corroding magnesium-based materials exposed to aqueous environments by SECM, Electrochem. Commun. 26 (2013) 25–28.
29. M. Taryba, S.V. Lamaka, D. Snihirova, M.G.S. Ferreira, M.F. Montemor, W.K. Wijting, S. Toews, G. Grundmeier, The combined use of scanning vibrating electrode technique and micro-potentiometry to assess the self-repair processes in defects on "smart" coatings applied to galvanized steel, Electrochim. Acta 56 (2011) 4475–4488.

30. A. Kiss, D. Filotás, R.M. Souto, G. Nagy, The effect of electric field on potentiometric scanning electrochemical microscopic imaging, Electrochem. Commun. 77 (2017) 138-141.
31. D.R. Curtis, A method for assembly of "parallel" micro-pipettes, Electroencephalogr. Clin. Neurophysiol. 24 (1968) 587–589.
32. B. Carette, A new method of manufacturing multi-barrelled micropipettes with projecting recording barrel, Electroencephalogr. Clin. Neurophysiol. 44 (1978) 248–250.
33. A.R. Crossman, R.J. Walker, G.N. Woodruff, Problems associated with iontophoretic studies in the caudate nucleus and substantia nigra, Neuropharmacology 13 (1974) 547–552.
34. C. Nicholson, Ion-selective microelectrodes and diffusion measurements as tools to explore the brain cell microenvironment, J. Neurosci. Met. 48 (1993) 199–213.
35. N. Fedirko, N. Svichar, M. Chesler, Fabrication and use of high-speed, concentric $H^+$- and $Ca^{2+}$-selective microelectrodes suitable for in vitro extracellular recording, J. Neurophysiol. 96 (2006) 919–924.
36. G. Somjen, R. Dingledine, B. Connors, B. Allen, Extracellular potassium and calcium activities in the mammalian spinal cord, and the effect of changing ion levels of mammalian neural tissues, in: Ion-Selective Microelectrodes and Their Use in Excitable Tissues, E. Sykova, (Ed.), Plenum Press, New York, 1981, pp. 159-180.
37. D. Filotás, B.M. Fernández-Pérez, J. Izquierdo, L. Nagy, G. Nagy, R.M. Souto, Combined amperometric/potentiometric probes for improved chemical imaging of corroding surfaces using scanning electrochemical microscopy, Electrochim. Acta 221 (2016) 48–55.
38. D. Filotás, B.M. Fernández-Pérez, J. Izquierdo, L. Nagy, G. Nagy, R.M. Souto, Novel dual microelectrode probe for the simultaneous visualization of local $Zn^{2+}$ and pH distributions in galvanic corrosion processes, Corros. Sci. 114 (2017) 37-44.
39. D. Filotás, B.M. Fernández-Pérez, A.Kiss, L. Nagy, G. Nagy, R.M. Souto, Double barrel microelectrode assembly to prevent electrical field effects in potentiometric SECM imaging of galvanic corrosion processes, J. Electrochem. Soc. 165 (2018) C270-C277.
40. O.V. Karavai, A.C. Bastos, M.L. Zheludkevich, M.G. Taryba, S.V. Lamaka, M.G.S. Ferreira, Localized electrochemical study of corrosion inhibition in microdefects on coated AZ31 magnesium alloy, Electrochim. Acta 55 (2010) 5401–5406.

650 41. S.V. Lamaka, M. Taryba, M.F. Montemor, H.S. Isaacs, M.G.S. Ferreira, Quasi-
651 simultaneous measurements of ionic currents by vibrating probe and pH distribution by ion-
652 selective microelectrode, Electrochem. Commun. 13 (2011) 20–23.
653 42. A. Alvarez-Pampliega, S.V. Lamaka, M.G. Taryba, M. Madani, J. De Strycker, E. Tourwé,
654 M.G.S. Ferreira, H. Terryn, Cut-edge corrosion study on painted aluminum rich metallic
655 coated steel by scanning vibrating electrode and micro-potentiometric techniques,
656 Electrochim. Acta 61 (2012) 107–117.
657 43. M.G. Taryba, M.F. Montemor, S.V. Lamaka, Quasi-simultaneous mapping of local current
658 density, pH and dissolved $O_2$, Electroanalysis 27 (2015) 2725–2730.
659 44. T. Yamamoto, Y. Oomura, H. Nishino, S. Aou, Y. Nakakao, Driven shield for multi-barrel
660 electrode, Brain Res. Bull. 14 (1985) 103-104.
661 45. B.R. Horrocks, M.V. Mirkin, D.T. Pierce, A.J. Bard, G. Nagy, K. Tóth, Scanning
662 electrochemical microscopy. 19. Ion-selective potentiometric microscopy, Anal. Chem. 65
663 (1993) 1213–1224.
664 46. F. Sjöberg, G. Nilsson, Dual mode antimony electrode for simultaneous measurements of
665 $pO_2$ and pH, Acta Anaesthesiol. Scand. 44 (2000) 32-36.
666 47. J. Izquierdo, L. Nagy, Á. Varga, J.J. Santana, G. Nagy, R.M. Souto, Spatially resolved
667 measurement of electrochemical activity and pH distributions in corrosion processes by
668 scanning electrochemical microscopy using antimony microelectrode tips, Electrochim. Acta
669 56 (2011) 8846-8850.
670 48. C. Wei, A.J. Bard, I. Kapui, G. Nagy, K. Tóth, Scanning electrochemical microscopy, 32.
671 Gallium ultramicroelectrodes and their application in ion-selective probes, Anal. Chem. 68
672 (1996) 2651–2656.
673 49. Y.Y. Lur'e, Handbook of Analytical Chemistry (In Russian, Spravochnik po Analiticheskoi
674 Himii), 6th edn., Himiya, Minsk, 1989.
675 50. S.V. Lamaka, R.M. Souto, M.G.S. Ferreira, In-situ visualization of local corrosion by
676 scanning ion-selective electrode technique, in: Microscopy: Science, Technology,
677 Applications and Education, Vol. 3., A. Méndez-Vilas, J. Díaz (Eds.), Formatex, Badajoz,
678 2010, pp. 2162-2173.

679 51. G. Williams, H. ap Llwyd Dafydd, R. Grace, The localised corrosion of Mg alloy AZ31 in
680 chloride containing electrolyte by a scanning vibrating electrode technique, Electrochim.
681 Acta 109 (2013) 489-501.
682 52. M. Curioni, The behavior of magnesium during free corrosion and potentiodynamic
683 polarization investigated by real-time hydrogen measurement and optical imaging,
684 Electrochim. Acta 120 (2014) 284-292.
685 53. N. Birbilis, A.D. King, S. Thomas, G.S. Frankel, J.R. Scully, Evidence for enhanced
686 catalytic activity of magnesium arising from anodic dissolution, Electrochim. Acta 132
687 (2014) 277-283.
688 54. I. Marco and O. Van der Biest, Polarization measurements from a rotating disc electrode for
689 characterization of magnesium corrosion, Corros. Sci. 102 (2015) 384-393.
690 55. S. Fajardo, C.F. Glover, G. Williams, G.S. Frankel, The source of anodic hydrogen
691 evolution on ultra high purity magnesium, Electrochim. Acta 212 (2016) 510-521.
692 56. S. Fajardo, G.S. Frankel, A kinetic model explaining the enhanced rates of hydrogen
693 evolution on anodically polarized magnesium in aqueous environments, Electrochem.
694 Commun. 84 (2017) 36-39.
695 57. G. Williams, N. Birbilis, H.N. McMurray, The source of hydrogen evolved from a
696 magnesium anode, Electrochem. Commun. 36 (2013) 1-5.
697 58. M. Taheri, J.R. Kish, N. Birbilis, M. Danaie, E.A. McNally, J.R. McDermid, Towards a
698 physical description for the origin of enhanced catalytic activity of corroding magnesium
699 surfaces, Electrochim. Acta 116 (2014) 396-403.
700 59. S. Thomas, N.V. Medhekar, G.S. Frankel, N. Birbilis, Corrosion mechanism and hydrogen
701 evolution on Mg, Curr. Opin. Solid State Mater. Sci. 19 (2015) 85-94.
702 60. D. Filotás, B.M. Fernández-Pérez, J. Izquierdo, A. Kiss, L. Nagy, G. Nagy, R.M. Souto,
703 Improved potentiometric SECM imaging of galvanic corrosion reactions, Corros. Sci. 129
704 (2017) 136-145.
705

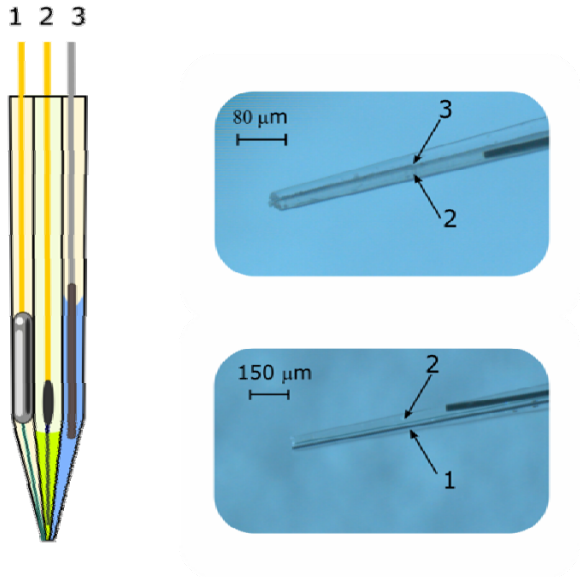


706

707 **Figure 1.** Sketch and photographs of the triple-barrel microelectrode assembly designed for
708 potentiometric SECM imaging. 1, pH-sensitive antimony electrode; 2, $Mg^{2+}$ selective
709 microelectrode; 3, Ag/AgCl micro-reference electrode.

710

711

712

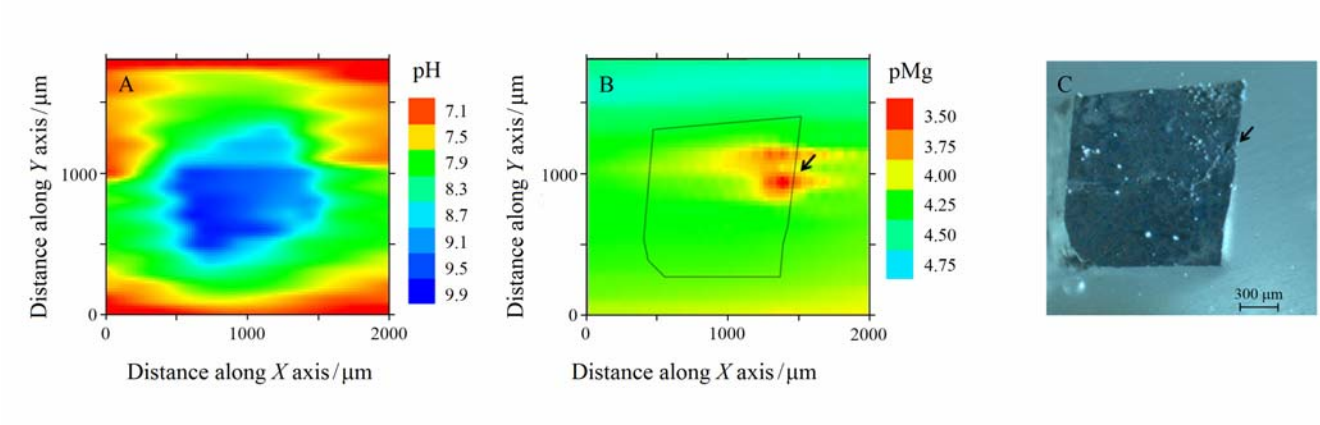


713

714 **Figure 2.** (A) pH and (B) pMg maps recorded above a spontaneously corroding AZ63 sample
715 immersed in 1 mM NaCl. (C) Optical micrograph of the AZ63 retrieved from the electrolyte
716 immediately after recording the pMg map shown in (B). The arrows in (B) and (C) indicate the
717 approximate location of the dark feature observed in the micrograph. Distance between the probe
718 and the sample: 20 µm; step size, 50 µm; scan rate, 17 µm $s^{-1}$.

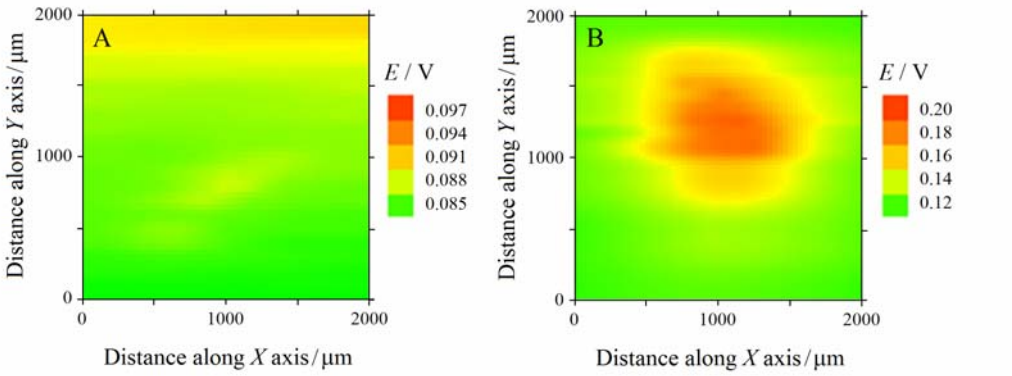


**Figure 3.** Potential distribution maps recorded above an AZ63 sample immersed in 1 mM NaCl. Electrical condition of the AZ63 sample: (A) spontaneously corroding at its rest potential; (B) galvanically coupled to iron. The scanning probe was an Ag/AgCl/(0.1 M) KCl micro-reference electrode, and its potential was measured with respect to a conventional Ag/AgCl/(3M) KCl reference electrode placed in the bulk of the electrolyte. Diameter of the micro-reference electrode probe: 15 µm; separation between AZ63 and Fe strips: 5 mm; distance between the probe and the sample: 20 µm; step size, 50 µm; scan rate, 20 µm $s^{-1}$.

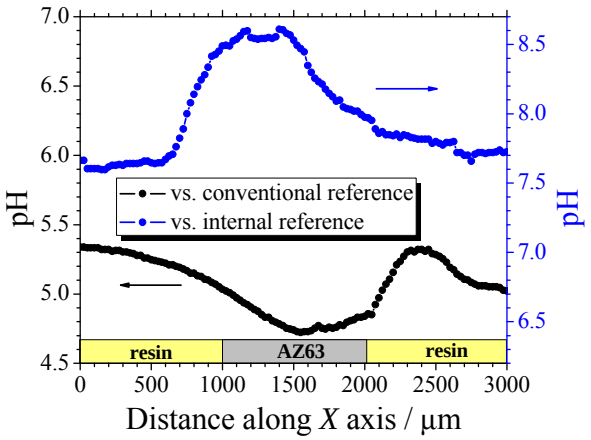


**Figure 4.** pH distribution line scans recorded above the AZ63 strip of an AZ63-Fe galvanic pair immersed in 1 mM NaCl. The black line was measured with the antimony ME in the double-barrel body with respect to a conventional Ag/AgCl/(3M) KCl reference electrode placed in the bulk of the electrolyte. Subsequently, the measurement was repeated while the potential values of the antimony ME were measured against the micro-reference electrode inserted in the double-barrel electrode assembly. Distance between the probe and the sample: 20 µm; step size, 50 µm; scan rate, 17 µm $s^{-1}$.

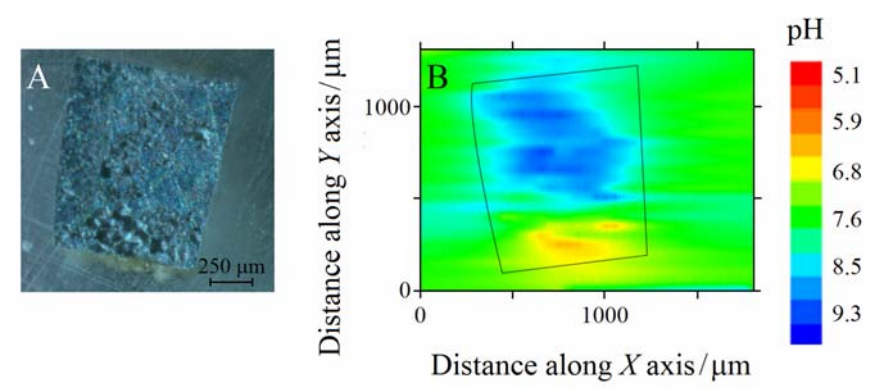


737
738 **Figure 5.** (A) Optical micrograph and (B) pH distribution map taken above the AZ63 strip of an
739 AZ63-Fe galvanic pair immersed in 1 mM NaCl. The localized pH measurements were
740 performed using a double-barrel probe containing an antimony ME and an Ag/AgCl micro-
741 reference electrode. Distance between the probe and the sample: 20 µm; step size, 50 µm; scan
742 rate, 17 µm $s^{-1}$.
743
744
745
746

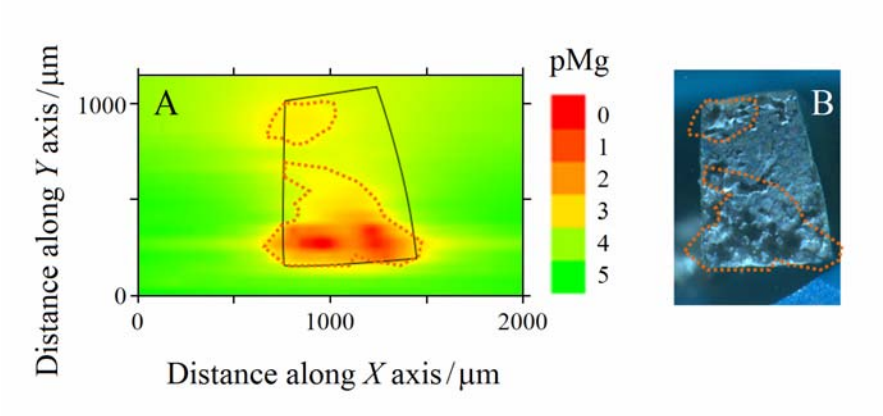


747
748 **Figure 6.** (A) pH distribution map and (B) optical micrograph taken above the AZ63 strip of an
749 AZ63-Fe galvanic pair immersed in 1 mM NaCl. The localized pMg measurements were
750 performed using a double-barrel probe containing a solid-contact Mg ion-selective ME and an
751 Ag/AgCl micro-reference electrode. Distance between the probe and the sample: 20 µm; step
752 size, 50 µm; scan rate, 17 µm $s^{-1}$.

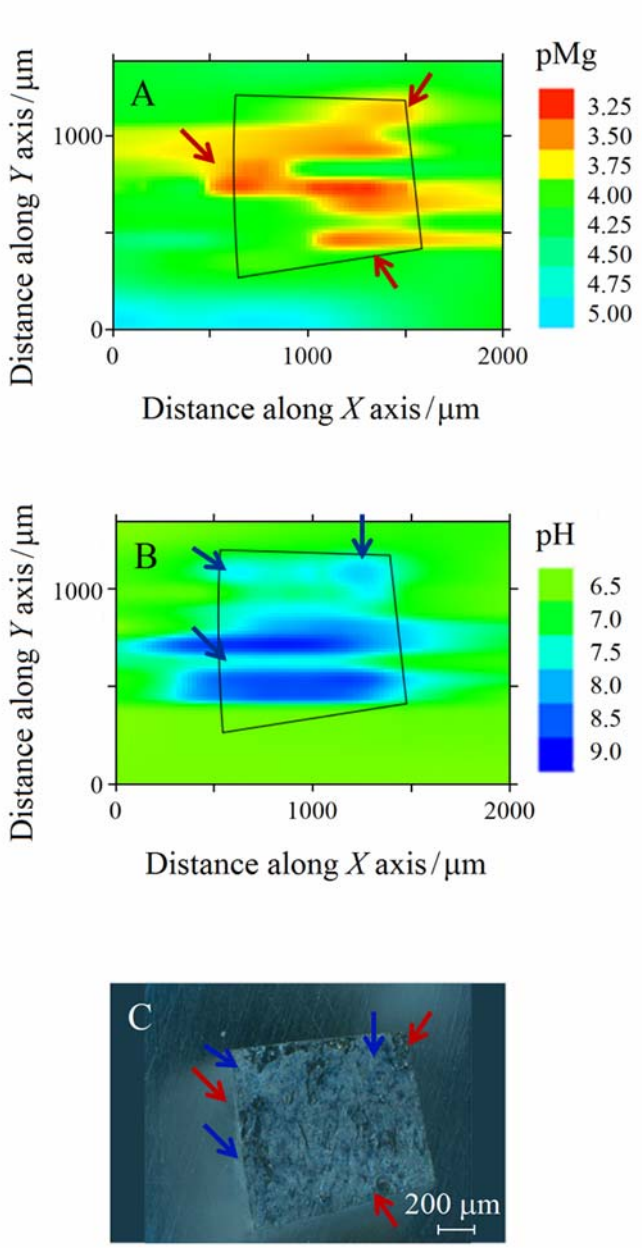


753
754 **Figure 7.** Simultaneous imaging of (A) $Mg^{2+}$ and (B) pH distributions above a spontaneously
755 corroding AZ63 strip immersed in 1 mM NaCl obtained. They were recorded using the novel
756 triple-barrel probe that contains a solid-contact Mg ion-selective ME, an antimony ME and an
757 Ag/AgCl micro-reference electrode. Distance between the probe and the sample: 20 µm; step
758 size, 50 µm; scan rate, 17 µm $s^{-1}$. (C) Optical micrograph taken above the AZ63 strip after
759 recording the SECM maps shown in (A) and (B). The arrows drawn in the pictures assist the
760 comments made in the text.
761

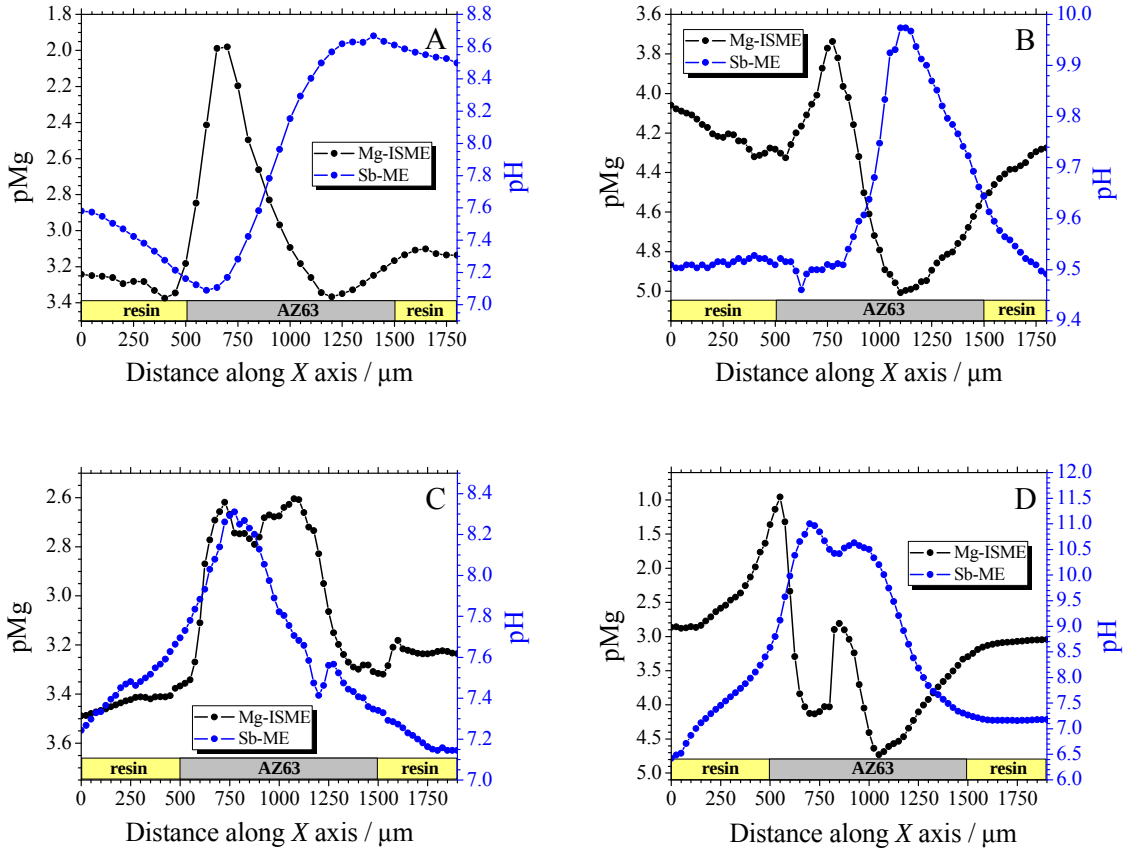


**Figure 8.** Selected line scans displaying $Mg^{2+}$ and pH distributions occurring above the AZ63 strip of an AZ63-Fe galvanic pair immersed in 1 mM NaCl. The line scans were recorded using the novel triple-barrel probe that contains a solid-contact Mg ion-selective ME, an antimony ME and a Ag/AgCl micro-reference electrode. Distance between the probe and the sample: 20 µm; step size, 50 µm; scan rate, 17 µm $s^{-1}$.